Development of an experimental apparatus for flat plate drag measurements and considerations for such measurements

OPEN ACCESS
IOP Publishing
Measurement Science and Technology
Meas. Sci. Technol. **33** (2022) 055303 (12pp)
https://doi.org/10.1088/1361-6501/ac527f

Development of an experimental apparatus for flat plate drag measurements and considerations for such measurements

M van Nesselrooij[1,2,*], O W G van Campenhout[1,2], B W van Oudheusden[1], F F J Schrijer[1] and L L M Veldhuis[1]

[1] Faculty of Aerospace Engineering, TU Delft, Kluyverweg 1, 2629 HS Delft, The Netherlands
[2] Dimple Aerospace B.V., Kluyverweg 1, 2629 HS Delft, The Netherlands

E-mail: m.vannesselrooij@tudelft.nl

Received 21 September 2021, revised 24 December 2021
Accepted for publication 7 February 2022
Published 23 February 2022

Abstract

Accurately measuring small changes in aerodynamic drag over a flat surface stands at the core of the development of technologies capable of reducing turbulent friction drag. A wind tunnel drag measurement system was developed which improves significantly on the state of the art. Experimental tests demonstrated that an uncertainty of less than 0.5% of C_D at a 95% confidence level was typically achieved, already at drag values below 1 N. This was replicated in two different wind tunnels. A match with literature on riblet performance within 1% of C_D was obtained. A crucial aspect of the design is the implementation of a correction for the pressure forces on the streamwise-facing surfaces of the test plate assembly. The flexible architecture of the system in the present realisation makes it suitable for most wind tunnels having a test section width of 400 mm or larger, which allows for accelerated development of turbulent drag reduction concepts from moderate-size low-cost facilities towards flow conditions relevant to the intended industrial application.

Keywords: aerodynamics, turbulent drag, force balance measurements, hot-wire anemometry

(Some figures may appear in colour only in the online journal)

1. Introduction

Skin friction drag from turbulent flow over flat surfaces accounts for a significant fraction of energy expenditure in many technology domains that contribute greatly to global greenhouse gas emissions, including aviation, maritime transport, high-speed rail, and hydrocarbon transmission pipelines.

The clear economic and environmental impact of reducing turbulent skin friction has motivated research on a large variety of concepts for many decades. The best-known and most successful example being shark skin-inspired riblets, for which the potential for drag reductions of 5%–10% has been well-established under laboratory conditions [1, 2]. Despite some success even in a full-scale flight test by Airbus in the early 1990s with riblet foil produced by 3M [3], inherent practical implications have prevented a commercially viable application to date. Hence, the development of alternative drag-reducing concepts has remained a relevant field of research.

* Author to whom any correspondence should be addressed.

The highly stochastic and non-linear nature of turbulent flow limits the ability to model drag-reducing mechanisms with general-purpose turbulence models, as these rely on empirical data or smooth-wall assumptions. Direct numerical simulation (DNS) is a powerful tool for fundamental studies, but in practice it is limited to relatively small domains, low Reynolds numbers, and simple geometries to maintain a reasonable computational effort. The general validity of results is further complicated by sensitivity to the choice of boundary conditions and domain size [4]. Therefore, experimental testing has remained a necessary tool for validating the efficacy of new concepts. Experimental testing in a wind or water tunnel furthermore provides the potential to test large numbers of relatively large surfaces of complex geometry at high Reynolds numbers in a relatively short time.

Numerous drag measurement techniques are available to the experimentalist, for which excellent reviews are provided by Winter [5] and Fernholz *et al* [6]. There are essentially two approaches: local or direct drag measurements. For local measurements, boundary layer information from hot-wire anemometry or particle image velocimetry (PIV) can be used to analyse momentum loss or wall-normal shifts of the logarithmic layer to infer the shear force at the measurement location [7, 8], while Preston tubes provide a local measurement that relies on the validity of the logarithmic law-of-the-wall [6]. Alternatively, MEMS skin friction sensors can accurately measure the local skin friction with high spatial resolution [9]. Local measurements always carry the risk of incorrectly extrapolating the result from the local to the global condition, i.e. shear force versus drag. In its simplest form the measurement of the total drag force can be achieved by connecting a force sensor to the test specimen that is exposed to the flow.

Despite its advantages, attempts to directly measure turbulent drag are plagued by uncertainties and insufficient accuracy. This has two main reasons. Firstly, in view of experimental limitations, most development work on new concepts for turbulent skin friction reduction is performed in low-speed wind tunnels and water tunnels with a maximum freestream velocity typically below 50 and 10 m s^{-1} respectively [10, 11]. For a reasonably sized test surface this leads to small measured drag forces, typically less than a few Newtons [12–14]. Secondly, although the only force of interest is that exerted by the tangential shear on the surface exposed to the flow, in reality, any test specimen has a three-dimensional shape and requires some form of physical interface between the specimen and the force sensor. This creates an opportunity for unwanted contributions in the overall measured force, such as those created by gravity, mechanical losses in the suspension or interface, pressure differentials on streamwise-facing surfaces and friction on surfaces other than those exposed to the flow. Each unwanted force component potentially adds to the bias and random errors in the overall force measurement, which obscures the friction drag effect under investigation.

As early-stage research into novel technologies for turbulent drag reduction often starts with sub-optimal designs, the ability to confidently measure changes in drag on the order of 1% or less is of particular importance. The inability to do so, in view of insufficient accuracy in the drag measurement, has inhibited the development of several drag reduction technologies in the past. For example, Chernyshenko's intriguing analytical prediction of drag reduction by oblique wavy surfaces [16] was validated experimentally by Denison *et al* [12]. The result was inconclusive, lying within the 1%–2% limit of uncertainty of the experiment. The concept later showed a 0.6% drag reduction in a first DNS study [17], reviving interest in the topic and reiterating the need for a measurement method suitable for studying drag effects of this small magnitude.

Similarly, significant discrepancies between measurement systems in similar flow conditions have led to an inefficient development path for shallow dimples as a potential means of turbulent drag reduction, with results varying from -20% to $+1\%$ for similar dimple geometries [11, 13, 14, 18].

In the next sections, a measurement system is presented which has been designed with the specific purpose to swiftly and reliably investigate concepts for the reduction of turbulent skin friction drag with effects on the order of 0.5% or more.

2. Methodology

The objective of this study is the design and validation of a measurement system that optimises repeatability by limiting manual interaction and which can be installed quickly in most wind tunnels without significant modification of the tunnel or the drag measurement system. Setups where the test surface is mounted flush with the wind tunnel wall, such as the ones at the Walter Bassett Aerodynamics Laboratory [15] or the NASA Langley Research Facility [19], offer the clear advantage of a minimal disturbance to the flow, but lack flexibility in available flow conditions. A self-contained system was developed which combines this advantage with improved flexibility, combining the lessons learned from three preceding designs [13, 14, 20].

2.1. System architecture

The measurement system consists of three key elements: (a) the structure that holds the test plate, sensors and actuators (hereafter referred to as core), (b) volumetric extensions that help define the flow condition encountered by the test plate, and (c) the data acquisition system (DAQ) that interfaces with the sensors, actuators and the wind tunnel. Attachment points for extensions on all sides of the core enable various measurement configurations depending on the design of the wind tunnel and the research objective. The high-level architecture of the core is schematically depicted in figure 1 and different extension configurations are shown in figure 2. Unless stated otherwise, measurements presented here used the configuration shown in figure 2(a).

The core element of the system is placed on the floor of the wind tunnel. To prevent the transmission of vibrations from the tunnel into the system, the contact is made by twelve Shore 00-30 Sorbothane® vibration isolators which are adjustable in height. The core has a length of 1020 mm, span of 395 mm and height of only 30 mm to minimise the effect of a pressure gradient on the boundary layer upstream of the test plate when operating in a configuration with a leading edge ramp, such as

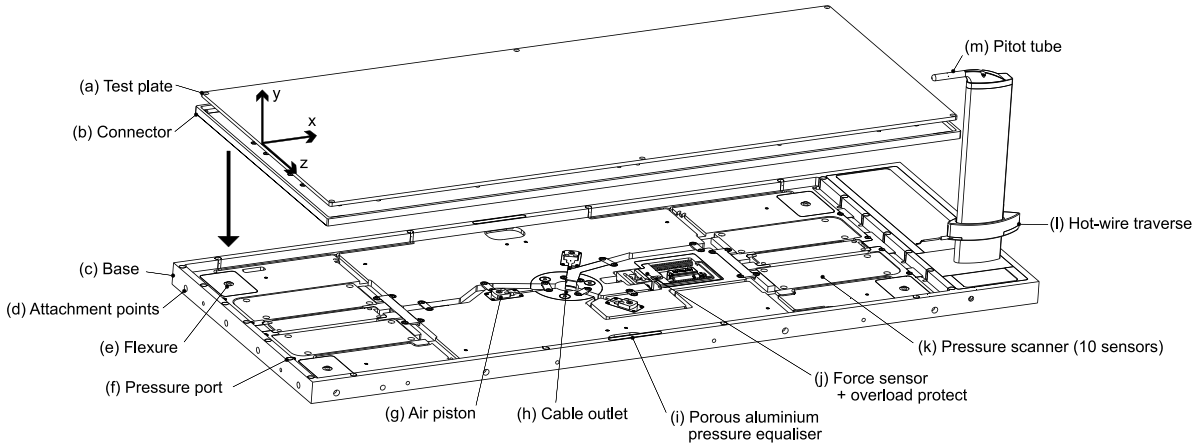

Figure 1. High-level architecture of the core element of the measurement system and definition of the reference frame.

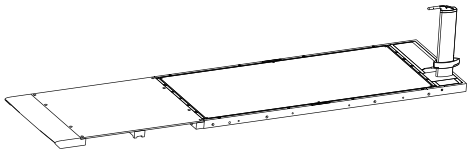

(a) Elliptical leading edge, with floor opening (expels tunnel boundary layer through floor)

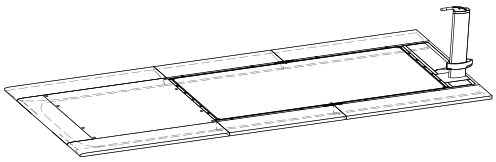

(b) Elliptical leading edge, without floor opening (guides the tunnel boundary layer below the setup)

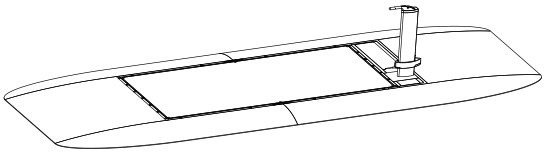

(c) Hill-like configuration (guides the tunnel boundary layer over the test surface)

Figure 2. Selection of alternative system configurations.

depicted in figure 2(c). The core accepts any test plate with a dimension of 881.3 mm $\times$ 366.3 mm $\times$ 5 mm and connects to the DAQ via a single wiring loom through the wind tunnel floor in the center of the system (item (h) in figure 1).

As the exposed surface of the test plate should be mounted flush with the top surface of the core and should be able to move freely, a gap must be maintained between the two. To eliminate the effect of production variance of the test plates on the size of this gap, a connector (item (b) in figure 1) provides a consistent interface between the fixed core base and the freely moving test plate. The core base and connector edge are both produced with a CNC milling process for a precise air gap of 0.3 mm $\pm$ 0.1 mm. The thickness of the floor of the connector was minimised to just 5 mm to maximise the available space for the test plate. However, this makes the connector susceptible to bending under the weight of heavier test plates and therefore the majority of the flat region of the connector was constructed from unidirectional carbon fibre reinforced polymer using Dialead XN60 high-modulus fibres.

In order to accurately measure the drag on the test plate, a sensitive force sensor is required which is unable to carry the vertical load due to the weight of the test plate. For this reason, the connector that holds the test plate is connected to the core via 0.3 mm thick titanium flexures in each of the four corners (item (e) in figure 1), with their direction of flexibility aligned with the freestream, so as to minimise their effect on the drag measurement. Different versions of the ME-systeme KD40S series force sensors ((j) in figure 1) are used, depending on the required range and accuracy. During all the measurements presented here, a $\pm$2 N range unit was installed. The small range of the force sensor presents the risk of overloading during installation, transportation or test plate insertion. Therefore, the sensor is automatically retracted by an electrical linear actuator after each measurement. When the sensor is engaged for measurement, springs ensure a firm connection between the sensor and the base of the core. In this position, the force sensor makes contact with a pin that extends from the bottom of the connector. The pin can be adjusted in the streamwise direction to ensure a small but positive force reading when the sensor is engaged and there is no flow.

With a test plate inserted in the connector, the top surfaces of the core, the connector and the test plate form a smooth surface to the flow. This complicates the manual removal of the test plate. Therefore, three miniature air pistons which are fed by compressed air are situated around the centre of the test plate (item (g) in figure 1). Small recesses in the connector allow the pistons to pass through to reach the test plate and push it upward for easy removal.

Variations in pressure throughout the air gap around the connector form a potential secondary drag force that

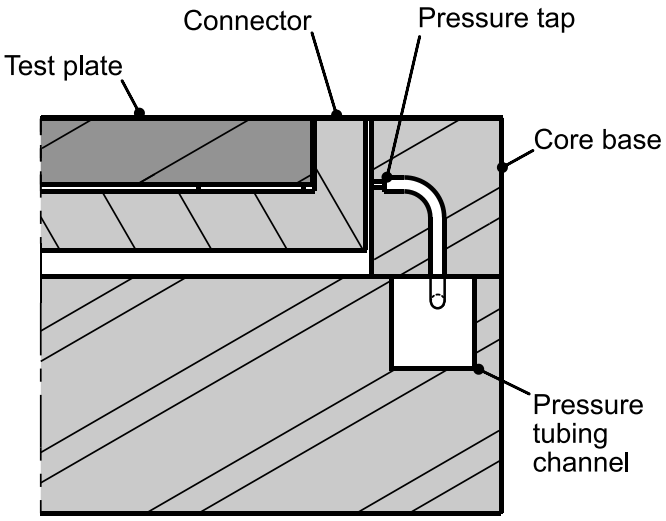

Figure 3. Simplified cross-sectional drawing indicating the position of a pressure tap in the air gap between the connector and base element of the core.

will be registered indiscriminately by the force sensor. The monitoring of these pressures and correcting for them is therefore an important aspect of the measurement system. Figure 3 shows a simplified schematic cross-section of a pressure tap installed in the trailing edge air gap. The taps are installed in the core mid-way ($y = -5$ mm) the height of the gap (10 mm) around the perimeter: seven in the leading edge gap, eight in the trailing edge gap, and four on each of the sides (item (f) in figure 1). The eighth tap on the trailing edge gap measures the vertical pressure variation in the gap at $z = 0$.

To monitor the streamwise static pressure gradient of the external flow, additional taps are installed on the top surface at locations of the pressure taps along the long edge of the test plate. To minimise the length of the pressure tubing, pressure scanners were developed in-house to fit inside the core of the system below the test plate (item (k) in figure 1). Four scanners with up to 10 Honeywell RSC sensors each provide temperature-compensated differential pressure data to the DAQ with a 2 kHz sampling rate at a full-scale span accuracy of 0.1% and a range of $\pm$250 Pa. Sensors with extended range are installed in one of the scanners to measure the total pressure from the pitot tube that is integrated in the system (item (m) in figure 1). For all measurements presented here, a $\pm$1245 Pa range sensor was used. The static pressure from the pitot tube is connected to the reference port on all pressure sensors.

As a result of the tight tolerance on the gap between the connector and the test plate, a fast drop in static pressure inside the wind tunnel during acceleration of the freestream (e.g. during start up of the tunnel) may result in a significant lift force on the test plate. To prevent lifting of the test plate, strips of porous aluminium in the edges of the core element on either side of the test plate form a pressure equalisation channel (item (i) in figure 1). In addition, the connector has six optional screw connections with the test plate as a safety precaution. The screw connections were not used in the measurements presented here.

Table 1. Overview of data signals.

Symbol	Signal	Origin	Rate (Hz)
F	Drag force	Core	25 000
p	Interior pressures	Core	2000
q	Dynamic pressure	Core	2000
U	Hot-wire voltage	Core	10 000
T	Temperature	Core	10
RH	Relative humidity	Core	10
p_a	Atmospheric pressure	DAQ	10

Knowledge of the flow conditions and specifically those within the boundary layer over the test plate is often a valuable extension of the force measurements. The system can provide this information with the use of the *data periscope* located downstream of the test plate. It combines a temperature and humidity sensor (IST HYT 939), hot-wire traverse system with a throw of 200 mm (item (l) in figure 1) and a pitot tube.

2.2. Data acquisition and processing

The DAQ collects and processes all signals from the core element of the system. It is controlled from a LabVIEW® program on a computer connected via USB, which has the option to simultaneously interface with the wind tunnel. Besides the custom electronics that interface with most sensors, the DAQ houses a Dantec Dynamics MiniCTA to control the hot-wire and a National Instruments cDAQ-9174 to read the analog signals from the force sensor and MiniCTA. Table 1 gives an overview of the signals output by the DAQ as well as their origins and sampling frequencies.

The velocity and unit Reynolds number can be calculated with the help of Buck's empirical relation for vapor pressure [21] from the relative humidity (RH), temperature (T), dynamic pressure (q) and absolute pressure (p_a) with equations (1)–(5), where $T_0 = 273.15$ K:

$$p_\upsilon = 0.61121 \times 10^{-3} RH \cdot exp\left[\frac{18.678 - T/234.84}{257.14 + T}\right], \quad (1)$$

$$\rho = \frac{0.028964(p_a - p_\upsilon) + 0.018016 p_\upsilon}{8.314(T + T_0)}, \quad (2)$$

$$\nu = \frac{4.18528 \times 10^{-4} \cdot (T + T_0)^{2.5}}{p_a \cdot (110.4 + T + T_0)}, \quad (3)$$

$$V = \sqrt{\frac{2q}{\rho}}, \quad (4)$$

$$Re = \frac{1 \cdot V}{\nu}. \quad (5)$$

The unit Reynolds number (i.e. Reynolds number based on a reference length of 1 m) is used here since a mix of concepts with different characteristic length scales will be compared throughout this work.

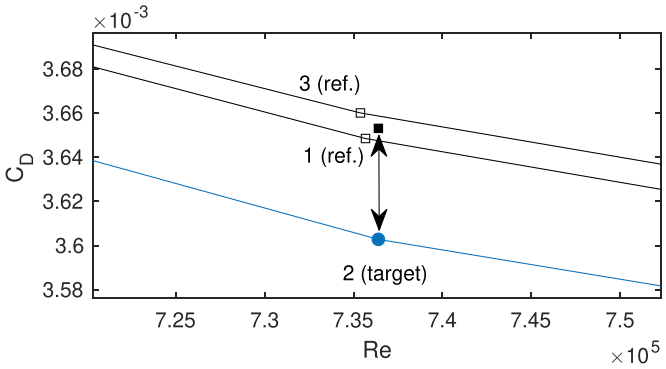

Figure 4. Example of referencing logic. The solid square indicates the reference C_D, based on interpolation and averaging of the reference velocity sweeps, while the arrow indicates the inferred drag reduction.

In order to calculate the drag coefficient based on the force measurement (C_{D_F}), the raw force signal should first be corrected by the change in the measured force before and after the velocity sweep with the wind tunnel turned off and V = 0 (ΔF_{null}). See equation (6), where S is the test plate surface (0.32 m^2). This change in null force is a very small effect caused by sensor temperature sensitivity and creep, and is applied proportionally to the measured force. To minimise its influence, a rest period is maintained between velocity sweeps, as discussed in more detail in section 3.1.2.

The corrected drag coefficient (C_D) is found by subtracting the pressure drag coefficient (C_{D_p}), which compensates for the parasitic pressure drag F_p (see section 2.2.2 and equations (7) and (8)):

$$C_{D_F} = \frac{F - \Delta F_{null}}{q \cdot S}, \tag{6}$$

$$C_{D_p} = \frac{-F_p}{q \cdot S}, \tag{7}$$

$$C_D = C_{D_F} + C_{D_p}. \tag{8}$$

2.2.1. Referencing. To improve accuracy, all analyses are relative to a flat reference test plate. To this end, each measurement set consists of seven velocity sweeps of increasing freestream velocity. During sweeps number 1, 3, 5 and 7 the reference plate is installed, while the test plate of interest (the 'target') is installed during sweeps number 2, 4 and 6. Each of the target plate sweeps is compared with the average of the reference sweeps before and after it. As C_D can vary with Reynolds number, accuracy is improved by interpolating the reference measurements at the Reynolds number of the target measurement. Hereafter this procedure is referred to as referencing, an example is shown in figure 4.

2.2.2. Interior pressure mapping. Knowledge of the pressure distribution around and below the test plate and connector plays a key role in the accuracy of the measurements.

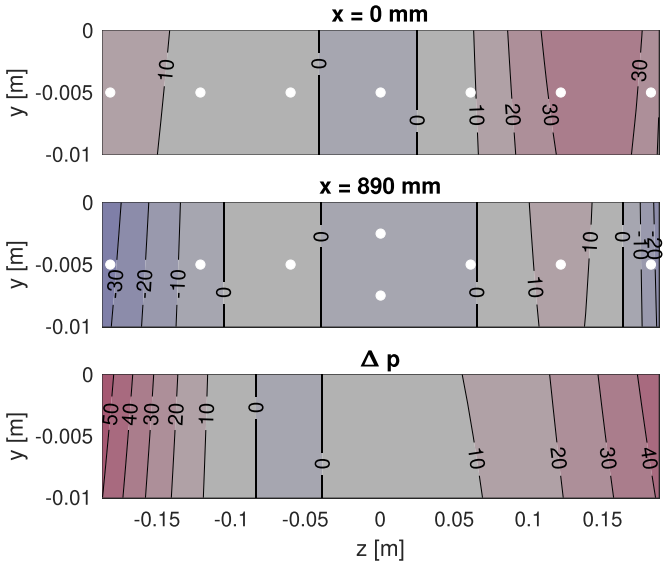

Figure 5. Example of measured leading edge ($x = 0$ mm) and trailing edge ($x = 890$ mm) gap pressures in N m^{-2} at $V \approx 35$ m s^{-1}, and the difference between the two (Δp). White circles indicate the locations of the pressure taps.

Therefore, 15 pressure taps are installed to map the pressure in the leading and trailing edge air gap. Two pressure taps in the centre ($z = 0$) of the trailing edge gap at $y = -2.5$ mm and $y = -7.5$ mm measure the pressure gradient in y-direction. This gradient is superimposed on all measured positions within the gap. An example result indicating the pressure tap locations is shown in figure 5, displaying the typical larger pressure readings near the edges and the (weak) effect of the data periscope stagnation pressure off-centre at the trailing edge. In addition, pressure taps in each of the four flexures are used to map the pressure gradient below the connector and applies a correction for its impact on the limited number of streamwise-facing surfaces in this area (e.g. the holes for the air pistons).

2.2.3. Hot-wire operation. The hot-wire is calibrated before each boundary layer measurement with a wind tunnel velocity sweep. When performing the calibration, the hot-wire is located in the uppermost position, such that it is outside of the boundary layer. Bruun's temperature compensation method [22] is applied to account for temperature variations between the calibration and the measurements. To strike an effective balance between speed and resolution, the boundary layer is sampled at 100 y-locations, with 50 locations evenly spaced over the lowest 25% of the boundary layer, 25 locations in the next 25%, and 25 locations in the upper 50%.

The robust boundary layer characterisation procedure by Rodríguez-López *et al* [23] is employed to address the uncertainty in the wall position and to obtain the most relevant boundary layer properties. A minor modification to the method is applied in the form of a more precise expression of the relation between the Von Kármán constant κ and the integration constant B of the logarithmic description of the boundary

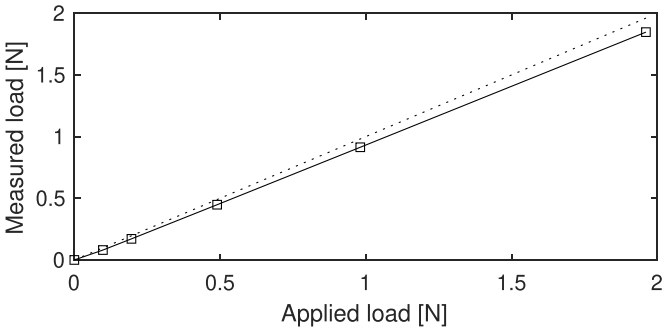

Figure 6. Load calibration result. The expected linear deviation from the dotted line ($x = y$) caused by the flexures is clearly visible.

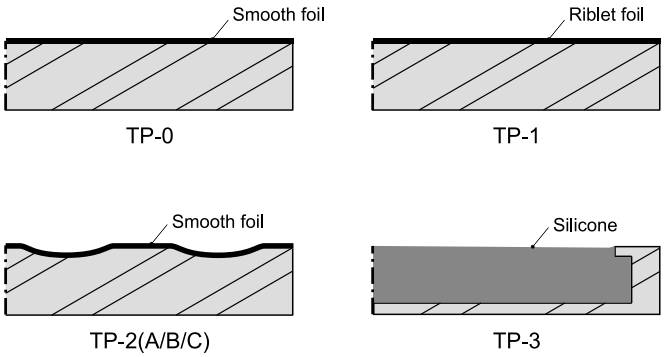

Figure 7. Schematic cross-sectional drawings of the used test plates. All plates have a total thickness of 5 mm.

layer, originally proposed by Nagib *et al* [24]. The new expression is given by:

$$\kappa B = 1.58086 \cdot (e^{0.1663B} - 1). \tag{9}$$

2.3. Force calibration

The use of flexures as a support mechanism for the test plate assembly necessitates a calibration of the force sensor signal to the horizontal drag force, since the elasticity of the flexures will partially resist this force. Figure 6 shows the result of the calibration using a pulley and calibrated weights. To minimize friction, the pulley has a sharp contact point with its axis instead of a bearing. The results show a linearly increasing deviation from the applied load caused by the resistance from the flexures. The force sensor reaches its rated bending displacement of 0.2 mm at a load of 2 N, at which the flexures carry a (drag) load of 0.11 N, or 5.5%.

The temperature dependence of this effect is negligible for typical wind tunnel measurements, given the Young's modulus variation of titanium of roughly 0.05% K^{-1} at 20 C, and hence $\delta F/\delta T \approx 0.003\%\ K^{-1}$.

2.4. Test plates

Four types of test plates were used to validate the measurement system, as schematically depicted in figure 7. The reference for all measurements is a 5 mm thick aluminium plate with a flat top surface made with an industrial CNC milling process (TP-0). The exposed top surface was wrapped with a smooth matte black foil to eliminate potential surface texture left by the milling process and to provide a non-reflecting surface for future use with PIV. For optimal flatness, the plate was constructed from tooling plate (SALPLAN 5000) for its low level of internal stresses, and was straightened with a roll press after milling.

In a benchmark test for future drag reduction studies, a duplicate of the flat plate was manufactured where the smooth foil was replaced by 3 M Scotchcal High Performance Film with saw-tooth riblets (TP-1). The riblets have a spanwise peak-to-peak spacing $s = 120$ µm and peak-to-trough height of $h = 110$ µm. This foil was obtained from the same sheet as that described by Greidanus *et al* [25]. A scanning electron microscope (SEM) image of the tested riblet foil is presented in figure 8.

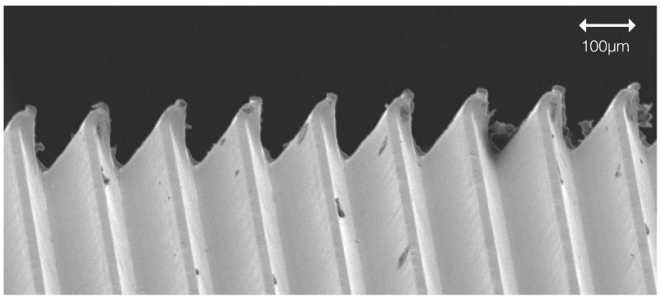

Figure 8. SEM picture of a sample of the tested riblet foil. Photo taken by D.P. Sharma (DASML, Delft University of Technology).

Table 2. Summary of tested dimple pattern designs.

Name	D	d/D	r/D	L_x/D	L_z/D	
TP-2A	20	2.5%	0.50	2.859	1.650	[13]
TP-2B	20	2.5%	0.50	1.650	2.859	[13]
TP-2C	50	5.0%	0.84	2.608	1.506	[26]

Non-flat surfaces are represented by an arbitrary selection of 3 test plates with spherical dimples (TP-2), manufactured with the same process as the reference plate. The dimple designs are based on those described by Tay *et al* [26] and van Nesselrooij *et al* [13] and are defined by their diameter (D), depth (d), edge rounding radius (r) and streamwise and spanwise spacing of dimple centres (L_x and L_z respectively). Table 2 summarises these parameters for the tested designs.

Lastly, as a variation to solid aluminium plates, the validations include a test plate comprising a large cavity into which silicone rubber was cast (TP-3). This type of plate could be used in the future to test compliant surfaces, which have shown drag reduction potential in DNS [27] and water experiments [28]. However, in the present context its purpose is primarily to assess the influence of weight of the test plate. Due to the properties of the silicone, this test plate introduces an appreciably different weight and surface texture, and has surface imperfections at the interface between the silicone and the aluminium ridge due to some degree of shortage or excess of silicone. The tested plate contained silicone with a high shear modulus

(approximately 40 kPa) for which it can be assumed that no two-way coupling with the air flow takes place in the tested flow conditions. Hence, the friction behaviour should be the same as for a rigid surface and any measured effects are to be attributed to the different weight and geometric properties.

2.5. Cavity suction

Some measurement systems employed by other authors, such as the S8Ch facility at ONERA described by Molton *et al* [29], use a suction pump to equalise the pressure in the cavities around and below the test plate. To test the efficacy of this approach for limiting the effect of the pressure distribution around and below the test plate, the measurement of TP-2A was repeated with a suction pump installed. The pump was attached to the sealed cable outlet at the centre of the system core element, establishing a pressure of −40 Pa in the gaps with the tunnel switched off. This pressure level was chosen to negate the highest pressures typically measured in the gap (see for example figure 5).

2.6. Measurement facilities

The results presented in the following sections were obtained from measurements with the system installed in two different wind tunnels. This involved that the setup was disassembled and reinstalled between these measurements. Unless otherwise stated, measurements were taken in the M-tunnel open-circuit wind tunnel facility with a test section of 400 × 400 mm, a maximum freestream velocity of approximately 35 m s^{-1} and a freestream turbulence intensity of approximately 0.7%. For validation, the similar open-circuit W-tunnel wind tunnel facility was used with a 400 × 400 mm test section, also reaching a maximum freestream velocity of 35 m s^{-1} and a freestream turbulence intensity of around 0.5%.

3. Results

An extensive number of tests were performed on the described measurement system to assess its capability to provide accurate, repeatable and reliable drag data. A summary of the drag measurements is provided in table 3. All measurement uncertainties are provided at a 95% confidence interval (CI), calculated as:

$$95\%\,\mathrm{CI} = \pm t_{0.975,n-1}\frac{\sigma}{\sqrt{n}}, \tag{10}$$

where σ is the standard deviation, n is the sample size, and t is the Student's t-distribution value that accounts for the small sample sizes under consideration [30].

3.1. Sensitivity analysis

Prior to the first drag comparisons, a range of tests were aimed at quantifying the sensitivity to common sources of inconsistencies in measurements.

Table 3. Summary of average measured drag difference with respect to TP-0 in normal orientation at the highest measured Reynolds number and the corresponding 95% confidence interval (CI) of the three measurements expressed as a percentage of $\overline{C_D}$. *rev.*: leading edge (LE) and trailing edge (TE) reversed. *LE/TE step*: test plate raised at its leading or trailing edge respectively to form a deliberate step for the flow.

Measurement	$\overline{\Delta C_D}$ (%)	95% CI (%)
TP-0	−0.07	±0.09
TP-0 (upside down)	−0.83	±0.30
TP-0 (rev.)	−0.68	±0.34
TP-0 (rev. & upside down)	−1.24	±0.23
TP-0 (LE step: 0.1 mm)	0.17	±0.37
TP-0 (LE step: 0.2 mm)	0.74	±0.28
TP-0 (LE step: 0.5 mm)	2.49	±0.55
TP-0 (TE step: 0.5 mm)	2.41	±0.64
TP-1	−3.48	±0.59
TP-2A	1.67	±0.21
TP-2A (Suction pump)	1.92	±0.46
TP-2A (W-tunnel)	2.21	±0.98
TP-2B	1.60	±0.31
TP-2B (W-tunnel)	1.82	±0.05
TP-2C	5.89	±0.21
TP-2C (W-tunnel)	6.22	±0.43
TP-3	−0.22	±0.31
TP-3 (rev.)	0.65	±0.58

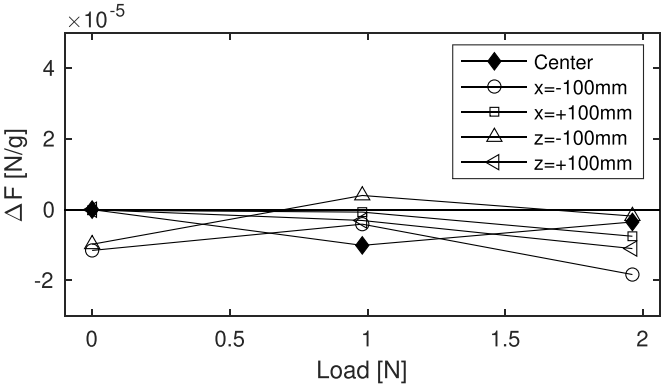

Figure 9. Variation in the linear weight dependence slope of the force signal for test plate weight increments at different locations for various horizontal calibration loads that imitate a drag force.

3.1.1. Test plate weight variation. The calibration of the force sensor described in section 2 was repeated with seven weights in increments of 25 g placed either in the centre of the test plate, or 100 mm in either direction on the streamwise and spanwise axis. As expected, the force reading has a linear dependence on the added weights caused at least in part by a gravitational component. The slope of this linear gradient was obtained for each case with a least squares fitting method. The slopes were then compared to the slope in the case where the weights were placed in the centre and no load was applied on the calibration wheel. This resembles how each velocity sweep is nulled prior to wind tunnel operation. Figure 9 shows that the variations are very minor and appear to be random. For example, for the centre load the deviation of the slope is less

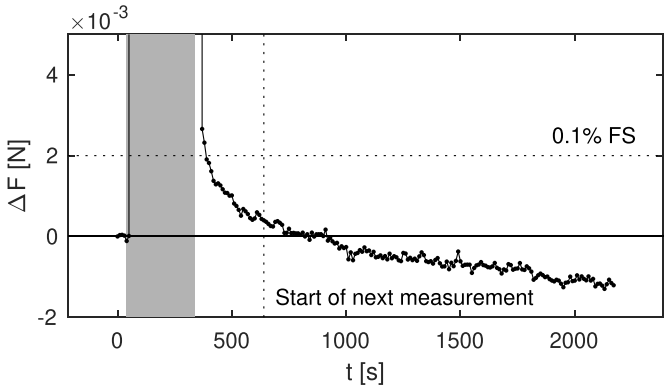

Figure 10. Force sensor creep test result. Grey area indicates the period of 2 N load application. Horizontal dotted line shows the 0.1% full-scale creep specified by the manufacturer. Vertical dotted line shows the preferred start of a next measurement.

than 10^{-5} N g^{-1}, meaning that for the dimpled plate, which is 30 g heavier than the reference plate, this error would be less than 3×10^{-4} N at 2 N (0.02%). Figure 9 further shows that the distribution of this weight variation should not have an error larger than twice this amount.

3.1.2. Sensor creep. The force sensor calibration was further extended to inspect the behaviour of the force signal output for a prolonged period after exposure to a full-scale load (2 N). The signal was continuously sampled for a 5 min full-scale load period, followed by 30 min at no load. Apart from pure sensor creep, this test also captures any creep-like effects from the flexures and temperature fluctuations (which were within one degree centigrade). The results are shown in figure 10. The sensor has a rated full-scale creep of 0.1% and indeed, the signal returns to the pre-load value within 2×10^{-3} N in under 30 s after release of the load. However, to further reduce the impact of the sensor creep on the measurement quality, any subsequent measurement is programmed to start automatically after 300 s when the unloaded signal is within 4×10^{-4} N of the pre-load value.

3.1.3. System levelness. Since a perfectly levelled measurement setup cannot be guaranteed, the sensitivity to inclination was investigated. With the flat reference test plate TP-0 installed, the system was levelled by adjusting the vibration-damping feet inside the core and using a digital inclinometer with an accuracy of 0.02 deg. It was then brought to an inclination of 0.2 degrees backward or forward by placing shims under the front or back feet respectively. The relatively high measurement uncertainty of this small rotation is acceptable, since the only requirement for observing a potential sensitivity to rotation is to achieve a constant, measurable change of angle. Drag measurements were taken during multiple velocity sweeps with the setup in each position. The significance of this small rotation is clearly reflected in the average force measured with the wind tunnel turned off: 0.25 N, 0.41 N and 0.62 N for the forward-leaning, levelled and backward-leaning position respectively. After applying the referencing procedure to these values, the trend in the velocity sweeps collapsed, leaving an uncertainty of 0.25% in $\overline{\Delta C_D}$ at $Re = 2 \times 10^6$. It should be noted that any sensitivity to inclination is not expected to translate into artificial drag contributions, as the inclination is unlikely to change between the measurement of the reference plate and the test plate of interest.

3.2. Measurement repeatability

A primary requirement for a reliable assessment of drag effects is having repeatable measurements. This was thoroughly scrutinised by testing only with the reference plate TP-0. The black squares in figure 11 show the result of a full set of seven velocity sweeps where TP-0 was removed and reinstalled identically for each measurement. It is clear from the right graph of figure 11 that all measurements lie well within 1% C_D. The average uncertainty is $\pm 0.5\%$ for $\mathrm{Re} > 1 \times 10^6$. At the highest measured velocity, the absolute value of the measured drag force is approximately 0.6 N on average, and the uncertainty is $\pm 0.09\%$.

It is interesting to note that in the bottom left graph of figure 11, the pressure correction for these measurements where the test plate is installed identically can hardly be distinguished ($<0.1\%$ C_D), thereby also validating the repeatability of the pressure measurements. Different behaviour is observed when the same plate TP-0 is compared against itself in different orientations by flipping it upside down, reversing the trailing and leading edge, or both. The results of these three additional measurement sets are also included in figure 11. With the bottom of the plate facing up, an increase in measured drag emerges, which is compensated by a pressure correction of up to 4%. Together this leads to a reduction of drag of 0.8% and 1.2% for the normal and reversed orientation respectively, with an uncertainty of $\pm 0.3\%$ or less.

Two likely contributors to this effect are the difference in surface roughness of the exposed aluminium bottom and the foil-covered top, and imperfect flatness of the plate (despite the efforts described in section 2). Surface roughness measurements indicate an average roughness $Ra \approx 1.5$ μm for the foil, and $Ra \approx 0.5$ μm for the cast aluminium surface. Both are at least an order of magnitude smaller than the minimum viscous length scale for the tested flow conditions ($l^+_{min} \approx 15$ μm) and thus no impact on the drag result should be expected [31].

It was found, however, that the depth of the cavity holding the test plate is slightly larger than 5 mm and that the test plate TP-0 has a small convexity in the spanwise direction. A dial gauge reveals that at the trailing and leading edge the actual test plate surface level of TP-0 in its normal orientation is $y \approx -0.2$ mm in the corners and $y \approx 0.0$ mm at the spanwise centre. As a consequence, the various rotations of the plate will alter the size and distribution of the steps between the connector and the test plate and thereby may explain the change in drag as well as the change in static pressure in the nearby gap registered by the pressure sensors.

To investigate this effect further, the same flat test plate TP-0 was tested in its normal orientation with shims of 0.1, 0.2 and 0.5 mm placed under the leading or trailing edge. Raising the test plate by 0.1 mm should yield a smaller step in the corners,

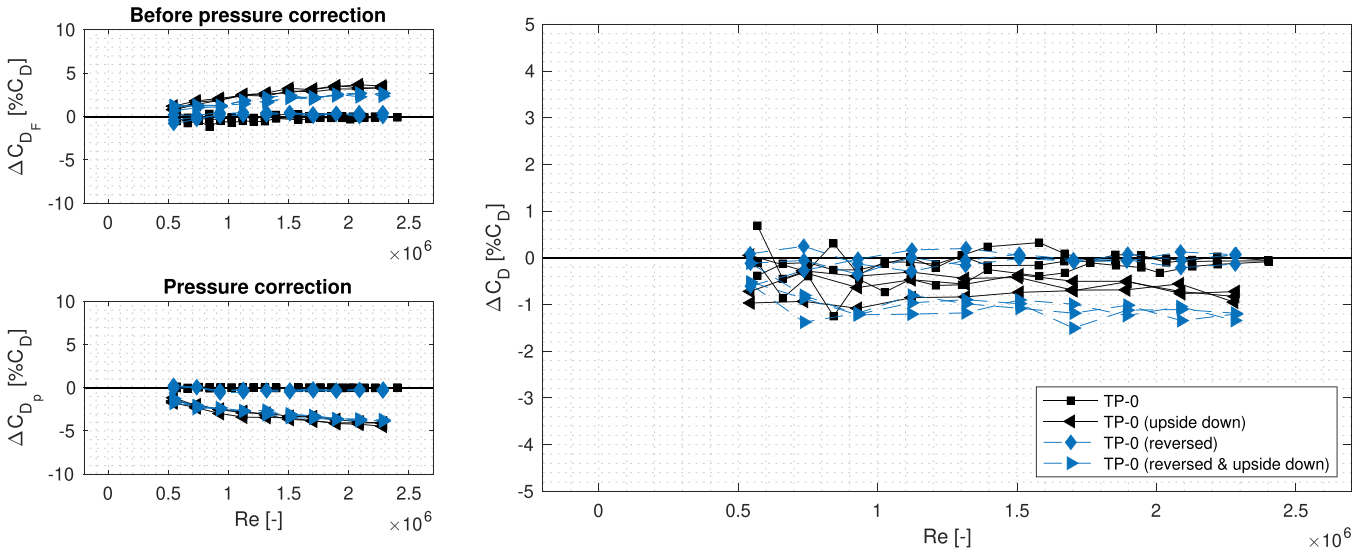

Figure 11. Measurement result overview of the flat reference plate TP-0 in four orientations, by rotation of 180 degrees over the x and y axes. The reference for each orientation is TP-0 in normal orientation. Top left: change in drag before pressure correction. Bottom left: pressure correction only. Right: final result by combining the results shown on the left.

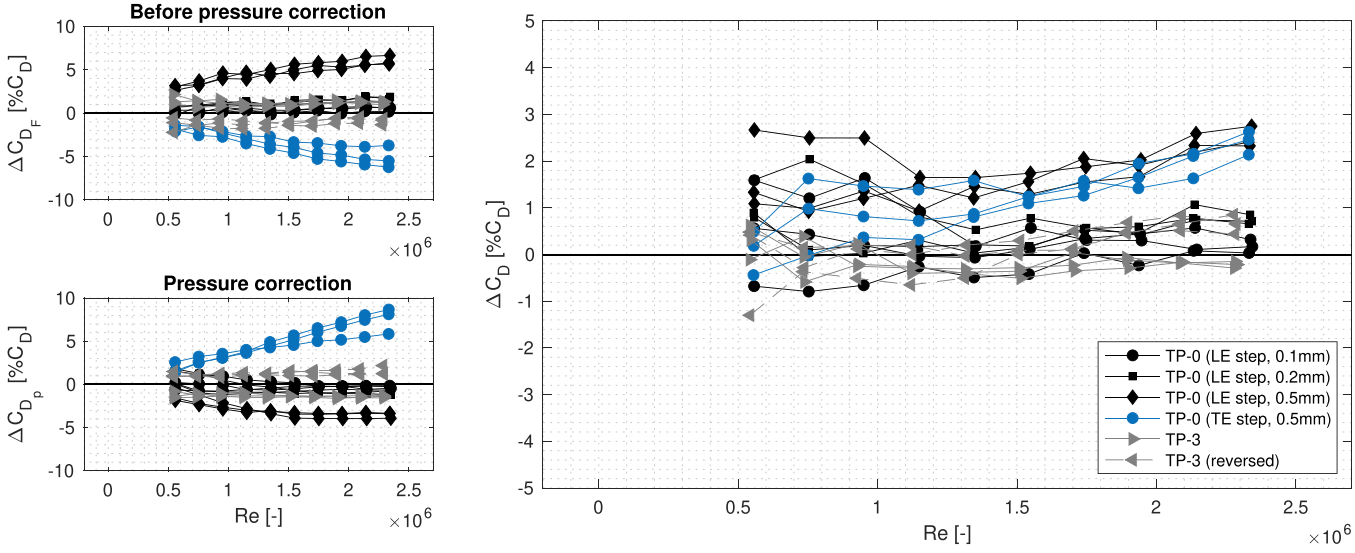

Figure 12. Measurement result overview of the silicone test plate TP-3 and the flat reference plate TP-0 with shims placed under the leading edge (LE) or trailing edge (TE) to create intentional forward or backward facing steps. Top left: change in drag before pressure correction. Bottom left: pressure correction only. Right: final result by combining the results shown on the left.

but introduces a minor step in the spanwise centre. Increasing to 0.2 mm, the test plate surface will lie above the connector surface with the exception of the corners. At 0.5 mm, the plate protrudes 0.3–0.5 mm into the flow along the span of the leading or trailing edge. The result of these measurements is presented in figure 12.

The mirrored nature of the graphs in the left of figure 12 is striking: measured increases in drag are accompanied by negative pressure corrections and vice versa. This is also consistent with figure 11. Indeed, it is not unexpected that for instance the stagnation on a forward-facing step at the leading edge increases the pressure in the nearby leading edge gap, effectively pushing the connector downstream and artificially amplifying the measured drag. After correcting for this, the remaining increase in drag can be attributed to the drag on the forward-facing step itself and its influence on the boundary layer downstream.

As expected, the 0.1 mm shim at the leading edge does not significantly influence the result, as the gap in corners is reduced at the expense of a new step near the centre. At 0.2 mm, a marginally significant drag penalty of 0.5%–1% with an uncertainty of $\pm$0.2%–0.6% is first obtained. With the 0.5 mm shims installed at the leading or trailing edge, the penalty already grows to a Reynolds number dependent increase of up to 3% C_D, with an uncertainty of $\pm$0.6%, in both cases. However, the consistency of these two results (i.e. increasing drag penalty with Reynolds number) is only achieved due to the pressure corrections of opposite sign.

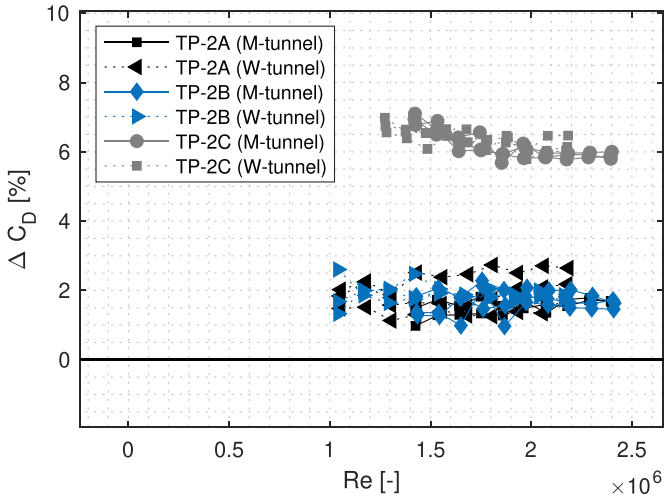

Figure 13. Measurement result of three test plates TP-2 (A/B/C) tested in two different wind tunnels.

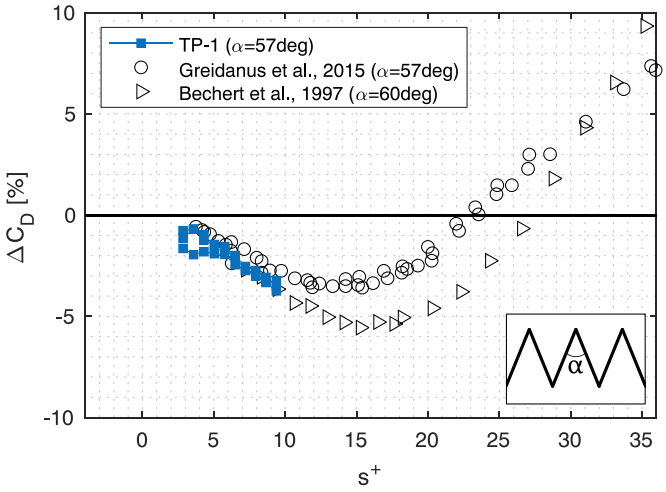

Figure 14. Comparison of the riblet test plate TP-1 with measurements by Greidanus *et al* [25] and Bechert *et al* [2] with similar ridge angle α.

Interesting to compare at this stage is the measurement result of the silicone test plate TP-3, which inevitably suffers from some degree of surface level imperfection at the interface between the silicone and the aluminium edge. Figure 12 includes the measurement result of TP-3 in its normal orientation, and for a 180 degree rotation over the y-axis. Again, the pressure corrections (shown in the bottom left of figure 12) mirror the trend in the uncorrected measurement (shown in the top left of figure 12), indicating the presence of a step, similar to the measurements with the deliberate steps. At the highest velocity, the average result is -0.2% C_D for the normal orientation, and 0.6% for the reversed orientation, which is comparable to the effect of a 0.2 mm leading edge step. Although it must be noted that these results lie within, or very close to, the uncertainty of the measurements (see table 3). The weight of TP-3 is approximately one third of the reference test plate, hence the limited magnitude of the measured drag difference again confirms the insensitivity to weight variation.

Beyond the investigation of test plate sensitivities, the measurement repeatability was validated by removing the setup from the wind tunnel, and installing it in the W-tunnel with similar flow conditions. Figure 13 shows the result of measuring the three dimpled test plates in both wind tunnels. A system configuration with a 450 mm long leading edge ramp, such as shown in figure 2(c), was used for these measurements due to the absence of a sufficiently large floor recess at the second wind tunnel to allow for expelling the wind tunnel boundary layer. Drag effects are reproduced to within 0.5% on average in the overlapping Reynolds number regime. It should be noted that although the wind tunnel characteristics are comparable, the similarity of the boundary layers at test plate leading edge ($x = 0$) in both tunnels, and thus the expected level of drag similarity, was not determined. However, with the reference test plate TP-0 installed, the velocity profiles obtained from the integrated traversing hot-wire located downstream of the test plate show typical characteristics for a turbulent boundary layer in both wind tunnels at a freestream velocity of approximately 31 m s^{-1}, with a similar thickness of approximately 23 and 26 mm for the M-tunnel and W-tunnel respectively.

Applying suction to the cavity below the test plate such that the pressures in the gap drop to -40 Pa with the wind tunnel turned off had little effect on the measurement result. As shown in table 3, the average drag increase from TP-2A changed by 0.25% C_D, which is within the uncertainty of these measurements. Moreover, although all pressure readings were lowered by 40 Pa, the change in pressure distribution with varying freestream velocity and location was affected little. For example, at the highest freestream velocity the average difference between the pressure in the leading and trailing edge gap was increased by approximately 6 Pa for TP-2A and 7 Pa for TP-0. This was caused by a slightly strengthened and weakened rise of gap pressure with freestream velocity for the leading and trailing edge gap respectively. A hypothesis for this behaviour is that with increasing freestream velocity, the suction effect on the leading edge gap becomes more pronounced due to the larger pressure differential between the pump and the higher-pressure leading edge gap. This could lead to an increased impingement of the flow on the vertical face of the connector in the gap. This hypothesis could not be confirmed with the pressure mappings, as the vertical pressure gradient is not resolved in the leading edge gap.

3.3. Riblet validation

As riblets are the most universally acknowledged passive method of turbulent drag reduction and are extensively characterised in literature, the riblet-covered test plate TP-1 serves here as a validation benchmark for testing the accuracy of the relative drag measurement. Figure 14 compares the result of seven velocity sweeps with reference data from literature, with on the horizontal axis the riblet spacing in viscous units $s^+ = su_\tau/\nu$. Here u_τ is determined for each velocity by applying the method by Rodríguez-López *et al* [23] on hot-wire boundary layer data for three freestream velocities, see

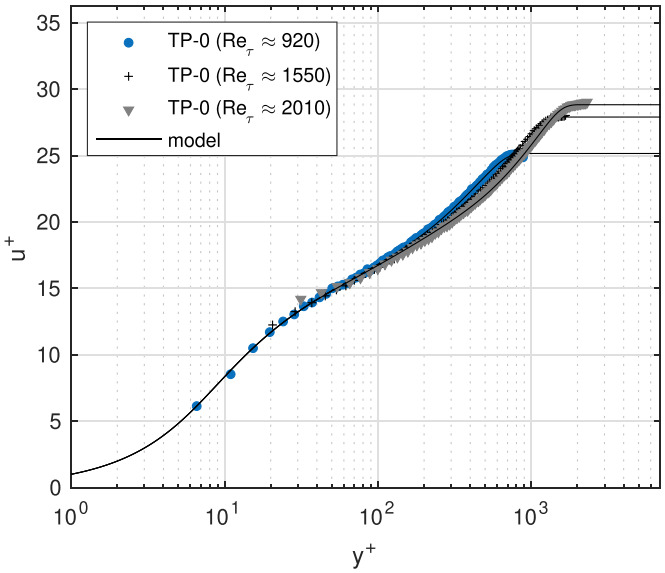

Figure 15. Mean velocity profiles acquired with a hot-wire at the trailing edge of test plate TP-0 at three different freestream velocities. Solid lines represent the best fit of the boundary layer model by Rodríguez-López *et al* [23] for each profile. $Re_\tau = u_\tau \delta / \nu$.

figure 15, assuming a linear relationship between U and u_τ. In agreement with results by other authors with similar riblet designs [2, 25], a drag reduction of up to 3.5% was consistently observed. Unfortunately, the maximum freestream velocity of the facility was insufficient to capture the location of optimal riblet performance for this design, which is expected to occur around $s^+ = 15$ [2].

4. Discussion

The overall goal of the measurements presented here is to characterise the performance of the described drag measurement system, in particular regarding the accuracy and repeatability of drag differences. At the highest measured freestream velocity of around 35 m s^{-1} the uncertainty is as low as 0.09% C_D when repeating measurements where the same test plate (TP-0) is placed in the same way every time. On average, the measurements reported in table 3 have four times less uncertainty than recently reported data at a similar flow velocity in the state-of-the-art facility at NASA Langley Research Center, reported by Spalart *et al* [11].

The accuracy of the measured drag difference is furthermore demonstrated by the good agreement between the riblet measurement results of TP-1 and the reference data from literature, even though there is a large variation in physical scale of the riblets and diverse testing configurations used. Specifically, the average of the new results deviates just 0.2% C_D from the oil channel results by Bechert *et al* [2], and 0.6% from the Taylor–Couette setup results by Greidanus *et al* [25].

Combined, the test results thus speak for the suitability and performance of the developed direct drag measurement system for the assessment of turbulent friction drag reduction technologies with effects on the order of 1% of C_D. It simultaneously demonstrates the subtleties involved in such assessments and the risk of misguidance, which has notoriously troubled this field of research.

For example, in measurement systems with an air gap between the test surface and its surroundings such as the one currently described, a correction for the pressure distribution in this gap is clearly necessary to obtain correct results. In fact, the current measurements show that without such a correction, the raise of 0.5 mm at trailing edge would lead to the incorrect conclusions that there is up to 5% drag reduction, while the same raise at the leading edge would suggest up to 6% drag increase. Correcting for the gap pressures distribution, both steps are shown to increase the drag by 1%–2.5%. It is realistic to expect that in any experiment of this type there can be local steps on the order of a few tenths of a millimetre, which would thus consistently affect outcomes to a significant degree.

Implementation of permeable patches near the test plate, as used in the current setup, are therefore deemed the preferred solution for pressure equalisation between the test section and the cavity below the test plate. Pressure distribution mapping can then accurately compensate for the inherent effect of pressure differentials in the air gap, while serving as a surface quality indicator.

The use of suction in the cavity below the test plate in an effort to limit the effect of the pressure distribution had little impact on the measurement results and did not improve the measurement quality. This can be understood by realising that the driving forces behind them (i.e. non-zero streamwise pressure gradient in the test section and steps at the test plate interface) are unaffected. Besides the more obvious disadvantages of added complexity, unintentional boundary layer suction and potential introduction of a source of uncertainty, this approach also underappreciates the added value of the gap pressure information as an indicator of surface quality.

5. Conclusions

A significant effort was made to develop and test a measurement system that is capable of measuring differences in turbulent drag on the order of a few percent in a wind tunnel with sufficient certainty. Scrutinising validation measurements confirmed that the design meets the necessary specifications. The 95% CI is typically less then 1% C_D, and regularly below 0.5% C_D when $Re > 2 \times 10^6$. Repeatability between wind tunnels was within 0.5% C_D on average for three test plate designs tested in two different wind tunnels. Comparing a benchmark test using riblets to measurements by leading authors suggest an accuracy on the order of 1% C_D or better.

It is worth noting that in addition to the performance and quality of the measurement system, the modular design and high level of automation of the system also satisfied the desire for fast testing of concepts. Acquiring three ΔC_D sweeps for a new design was typically accomplished within two hours. Installation and removal of the system was routinely performed in under one hour, enabling particularly efficient use of wind tunnel facilities.

With the performance of the current drag measurement system verified and quantified, it can be employed in future

studies to explore with improved certainty the potential for turbulent friction reduction for the array of promising concepts that have suffered from measurement uncertainties in the past.

Data availability statement

All data that support the findings of this study are included within the article (and any supplementary files).

Acknowledgments

This research has been funded by Dimple Aerospace B.V. Patent Application WO 2021/069676 A1 is directed at the described system and is owned by Dimple IP B.V. The authors kindly thank Herman Soemers for his counsel on the system architecture.

ORCID iDs

M van Nesselrooij https://orcid.org/0000-0002-4696-0408
O W G van Campenhout https://orcid.org/0000-0002-2411-7946
B W van Oudheusden https://orcid.org/0000-0002-7255-0867
F F J Schrijer https://orcid.org/0000-0002-7532-4320
L L M Veldhuis https://orcid.org/0000-0002-4869-8423

References

[1] Viswanath P R 2002 Aircraft viscous drag reduction using riblets *Prog. Aerosp. Sci.* **38** 571–600
[2] Bechert D W, Bruse M, Hage W, Van Der Hoeven J G T and Hoppe G 1997 Experiments on drag-reducing surfaces and their optimization with an adjustable geometry *J. Fluid Mech.* **338** 59–87
[3] Szodruch J 1991 Viscous drag reduction on transport aircraft *29th Aerospace Sciences Meeting*
[4] Fukagata K, Kern S, Chatelain P, Koumoutsakos P and Kasagi N 2008 Evolutionary optimization of an anisotropic compliant surface for turbulent friction drag reduction *J. Turbul.* **9** N35
[5] Winter K G 1979 An outline of the techniques available for the measurement of skin friction in turbulent boundary layers *Prog. Aerosp. Sci.* **18** 1–57
[6] Fernholz H H, Janke G, Schober M, Wagner P M and Warnack D 1996 New developments and applications of skin-friction measuring techniques *Meas. Sci. Technol.* **7** 1396–409
[7] Lee I, Kulik V M, Boiko A V and Chun H H 2009 Experimental investigation of drag reducing mechanism of compliant coating with optimal viscoelastic properties *6th Int. Symp. on Turbulence and Shear Flow Phenomena* (Begel House Inc.)
[8] Walters R R 1969 Turbulent boundary layer characteristics of flow over a compliant surface *PhD Thesis* The University of Oklahoma
[9] Jiang Z, Farmer K R and Modi V 2001 A MEMS device for measurement of skin friction with capacitive sensing *2001 Microelectromechanical Systems Conf. (Cat. No. 01EX521)* pp 4–7
[10] Greidanus A J, Delfos R and Westerweel J 2017 Fluid-structure interaction of compliant coatings under turbulent flow conditions: force and PIV analysis *AMT'17 Conf. Proc. Hydro Testing Forum*
[11] Spalart P R, Shur M, Strelets M, Travin A, Paschal K B and Wilkinson S P 2019 Experimental and numerical study of the turbulent boundary layer over shallow dimples *Int. J. Heat Fluid Flow* **78** 108438
[12] Denison M, Wilkinson S P and Balakumar P 2015 On the effect of rigid swept surface waves on turbulent drag *45th AIAA Fluid Dynamics Conf.* p 3221
[13] van Nesselrooij M, Veldhuis L L M, van Oudheusden B W and Schrijer F F J 2016 Drag reduction by means of dimpled surfaces in turbulent boundary layers *Exp. Fluids* **57** 142
[14] van Campenhout O W G, van Nesselrooij M, Veldhuis L L M, van Oudheusden B W and Schrijer F F J 2018 An experimental investigation into the flow mechanics of dimpled surfaces in turbulent boundary layers *2018 AIAA Aerospace Sciences Meeting (Kissimmee, Florida)*
[15] Baars W J, Squire D T, Talluru K M, Abbassi M R, Hutchins N and Marusic I 2016 Wall-drag measurements of smooth- and rough-wall turbulent boundary layers using a floating element *Exp. Fluids* **57** 90
[16] Chernyshenko S I 2013 Drag reduction by a solid wall emulating spanwise oscillations (arXiv:1304.4638)
[17] Ghebali S, Chernyshenko S I and Leschziner M A 2017 Can large-scale oblique undulations on a solid wall reduce the turbulent drag? *Phys. Fluids* **29** 105102
[18] Veldhuis L L M and Vervoort E 2009 Drag effect of a dented surface in a turbulent flow *27th AIAA Applied Aerodynamics Conf.* (*Fluid Dynamics and Co-Located Conferences*) (American Institute of Aeronautics and Astronautics)
[19] Roth J R, Sherman D M and Wilkinson S P 2000 Electrohydrodynamic flow control with a glow-discharge surface plasma *AIAA J.* **38** 1166–72
[20] van Weersch Y 2017 On the turbulent drag reduction of a dimpled surface under a pressure gradient *Master's Thesis* TU Delft, Aerospace Engineering
[21] Buck A L 1981 New equations for computing vapor pressure and enhancement factor *J. Appl. Meteorol. Climatol.* **20** 1527–32
[22] Bruun H H 1995 *Hot-Wire Anemometry* (Oxford: Oxford University Press)
[23] Rodríguez-López E, Bruce P J K and Buxton O R H 2015 A robust post-processing method to determine skin friction in turbulent boundary layers from the velocity profile *Exp. Fluids* **56** 68
[24] Nagib H M and Chauhan K A 2008 Variations of von Kármán coefficient in canonical flows *Phys. Fluids* **20** 101518
[25] Greidanus A J, Delfos R, Tokgoz S and Westerweel J 2015 Turbulent Taylor–Couette flow over riblets: drag reduction and the effect of bulk fluid rotation *Exp. Fluids* **56** 107
[26] Tay C M J, Khoo B C and Chew Y T 2015 Mechanics of drag reduction by shallow dimples in channel flow *Phys. Fluids* **27** 035109
[27] Józsa T I, Balaras E, Kashtalyan M, Borthwick A G L and Viola I M 2019 Active and passive in-plane wall fluctuations in turbulent channel flows *J. Fluid Mech.* **866** 689–720
[28] Choi K-S, Yang X, Clayton B R, Glover E J, Atlar M, Semenov B N and Kulik V M 1997 Turbulent drag reduction using compliant surfaces *Proc. R. Soc.* A **453** 2229–40
[29] Molton P, Hue D and Bur R 2015 Drag induced by flat-plate imperfections in compressible turbulent flow regimes *J. Aircr.* **52** 667–79
[30] Student 1908 The probable error of a mean *Biometrika* **6** 1–25
[31] Raupach M R, Antonia R A and Rajagopalan S 1991 Rough-wall turbulent boundary layers *Appl. Mech. Rev.* **44** 1–25